Adventures of a tidally induced bar

E. L. Łokas,[1]★ E. Athanassoula,[2] V. P. Debattista,[3] M. Valluri,[4] A. del Pino,[5] M. Semczuk,[6] G. Gajda[6] and K. Kowalczyk[1,7]

[1]*Nicolaus Copernicus Astronomical Center, Bartycka 18, PL-00-716 Warsaw, Poland*
[2]*Laboratoire d'Astrophysique de Marseille (LAM), UMR6110, CNRS/Université de Provence, Technopôle de Marseille Etoile, 38 rue Frédéric Joliot Curie, F-13388 Marseille Cédex 13, France*
[3]*Jeremiah Horrocks Institute, University of Central Lancashire, Preston PR1 2HE, UK*
[4]*Department of Astronomy, University of Michigan, Ann Arbor, MI 48109, USA*
[5]*Instituto de Astrofísica de Canarias, Calle Vía Láctea s/n, E-38200 La Laguna, Tenerife, Canary Islands, Spain*
[6]*Astronomical Observatory of the Jagiellonian University, Orla 171, PL-30-244 Cracow, Poland*
[7]*Warsaw University Observatory, Al. Ujazdowskie 4, PL-00-478 Warsaw, Poland*

ABSTRACT

Using *N*-body simulations, we study the properties of a bar induced in a discy dwarf galaxy as a result of tidal interaction with the Milky Way. The bar forms at the first pericentre passage and survives until the end of the evolution at 10 Gyr. Fourier decomposition of the bar reveals that only even modes are significant and preserve a hierarchy so that the bar mode is always the strongest. They show a characteristic profile with a maximum, similar to simulated bars forming in isolated galaxies and observed bars in real galaxies. We adopt the maximum of the bar mode as a measure of the bar strength and we estimate the bar length by comparing the density profiles along the bar and perpendicular to it. The bar strength and the bar length decrease with time, mainly at pericentres, as a result of tidal torques acting at those times and not to secular evolution. The pattern speed of the bar varies significantly on a time-scale of 1 Gyr and is controlled by the orientation of the tidal torque from the Milky Way. The bar is never tidally locked, but we discover a hint of a 5/2 orbital resonance between the third and fourth pericentre passage. The speed of the bar decreases in the long run so that the bar changes from initially rather fast to slow in the later stages. The boxy/peanut shape is present for some time and its occurrence is preceded by a short period of buckling instability.

Key words: galaxies: dwarf – galaxies: evolution – galaxies: interactions – galaxies: kinematics and dynamics – Local Group.

1 INTRODUCTION

Observations indicate that a significant fraction of spiral galaxies are barred (e.g. Cheung et al. 2013, and references therein). While precise measurements of the bar fraction vary (between 20 and 70 per cent, depending on the sample), there is no doubt that the phenomenon is a rather common feature in galaxies. In addition, comparisons of the frequency of bar presence in nearby galaxies to the one in high-redshift objects lead to the conclusion that bars occur relatively late in the evolution of galaxies (Sheth et al. 2008).

The essence of bar formation is the transformation of circular orbits in the stellar disc into elongated ones (for reviews on dynamics of bars see e.g. Sellwood & Wilkinson 1993; Athanassoula 2013).

While a simplified analytic description of the phenomenon is possible (Binney & Tremaine 2008), the problem can be fully tackled only using *N*-body simulations. This approach was pioneered by Miller & Smith (1979) who studied the bar evolution and discussed the bar pattern speed, the particle orbits and the predicted observational properties of bars. Sparke & Sellwood (1987) studied the bar formation via disc instability, performed detailed classification of stellar orbits in the bar and found the bar to be stable and robust. While such instability is indeed generally believed to be responsible for bar formation, we still do not have a full grasp of all the intricacies of bar formation and evolution and alternative ways to form a bar have been considered.

Combes et al. (1990) were among the first to discuss the box and peanut shapes generated by stellar bars and Raha et al. (1991) discovered a mechanism that may be responsible for these shapes in the form of the buckling instability. The instability drives the stars

★ E-mail: lokas@camk.edu.pl

out of the galactic plane and may significantly weaken the bar (for more recent developments see e.g. Athanassoula 2005; Martinez-Valpuesta, Shlosman & Heller 2006; Saha, Pfenniger & Taam 2013). Insight into its nature can be obtained via studies of vertical orbital instabilities (e.g. Binney 1978; Pfenniger 1984; Skokos, Patsis & Athanassoula 2002a,b).

Additional complication in the study of bar dynamics is introduced by the presence of extended dark matter haloes surrounding the discs (Debattista & Sellwood 2000; Athanassoula 2002, 2003; Dubinski, Berentzen & Shlosman 2009; Saha & Naab 2013). Overall, the evolution of the bar's major properties, such as its strength or pattern speed depends on a plethora of parameters and has been only partially explored in simulations (Athanassoula & Misiriotis 2002; Klypin et al. 2009; Athanassoula, Machado & Rodionov 2013).

One factor that has been relatively underexplored is the effect of galaxy interactions. Previous studies of the influence of interactions on the properties of the bars discussed mainly the effect of a satellite on the bar in the normal-size galaxy (Gerin, Combes & Athanassoula 1990; Sundin, Donner & Sundelius 1993; Miwa & Noguchi 1998; Mayer & Wadsley 2004; Romano-Díaz et al. 2008). In this paper we are interested in a different phenomenon, that of a tidally induced bar in a dwarf galaxy interacting with a bigger host. Important hints that such a process may be important in shaping the properties of present-day dwarfs are provided by observations that bars form later in fainter galaxies (Sheth et al. 2008) and that bar fraction is higher in fainter objects in dense environments such as galaxy clusters (Lansbury, Lucey & Smith 2014). A possible interpretation of these results is that dwarf galaxies are born with dynamically hotter discs which delays bar formation (Athanassoula & Sellwood 1986; Sheth et al. 2012) until they are accreted by a more massive galaxy or become a member of a group or cluster where they are affected by tidal forces. An example of such a tidally induced bar could be the one in M82, resulting from an interaction with M81 (Wills et al. 2000).

The formation of tidally induced bars in dwarf galaxies has been studied mainly in the context of the tidal stirring scenario for the formation of dwarf spheroidal (dSph) galaxies in the Local Group (Mayer et al. 2001; Klimentowski et al. 2009; Kazantzidis et al. 2011; Łokas, Kazantzidis & Mayer 2011). The simulations of this process revealed that the formation of a bar is a natural intermediate stage of a dwarf galaxy in its morphological evolution from a disc towards a spheroid that occurs for a variety of dwarf's orbits around the host and for different initial structural parameters. Łokas et al. (2012) measured the shapes of simulated dSph galaxies and compared them to the shapes of classical dSph satellites of the Milky Way quantified in the same way. Bar-like surface density distributions were found in the Sagittarius, Ursa Minor and possibly Carina dwarfs. Elongated shapes, suggestive of the presence of the bar are also seen in the recently discovered ultra-faint dwarfs like Hercules (Coleman et al. 2007) and Ursa Major II (Muñoz, Geha & Willman 2010). Note that although the Large Magellanic Cloud (LMC) is also known to possess a bar, this structure is probably not of tidal origin. Indeed, according to the most probable scenario the LMC is at its first pericentre around the Milky Way (Besla et al. 2007) and its pericentric distance is too large (50 kpc) for the tidal forces to be effective.

The Sagittarius dwarf seems to be the most obvious candidate for a barred galaxy among the Local Group dSphs. Łokas et al. (2010) proposed an evolutionary model of this dwarf starting from a disc embedded in a dark matter halo. After the first pericentre passage, the stellar component of the dwarf transforms into a bar that survives until the next pericentre which was identified as the

present stage of the dwarf we observe. The shape of the dwarf at this time matches very well the actual elongated shape determined from observations by Majewski et al. (2003). The model also explains the lack of rotation signal in the data (Frinchaboy et al. 2012).

In this work, we look in more detail into the properties of a tidally induced bar on a typical orbit around the Milky Way. In Section 2, we present the simulation used for this study. In Section 3, we describe the evolution of the dwarf galaxy using global measurements of its properties. Sections 4 and 5 focus on the strength and length of the bar, while Section 6 is devoted to the pattern speed of the bar and its interpretation. The discussion follows in Section 7.

2 THE SIMULATION

Our simulation set-up consisted of live models of two galaxies: the Milky Way-like host and the dwarf galaxy. The *N*-body realizations of both galaxies were generated via procedures described in Widrow & Dubinski (2005) and Widrow, Pym & Dubinski (2008). The procedures allow us to generate near-equilibrium models of galaxies composed of a disc, a bulge and a halo with required properties. Both our galaxies contained exponential discs embedded in NFW (Navarro, Frenk & White 1997) dark matter haloes. The dark haloes were smoothly truncated at the radius close to the virial radius in order to make their masses finite. Each component of each galaxy contained 10^6 particles (4×10^6 particles total).

The dwarf galaxy model was similar to the default model used in recent simulations of tidal stirring (Kazantzidis et al. 2011; Łokas et al. 2011). The dark halo of the dwarf had a mass $M_h = 10^9$ M$_\odot$ and concentration $c = 20$. The disc had a mass $M_d = 2 \times 10^7$ M$_\odot$, exponential scalelength $R_d = 0.41$ kpc and thickness $z_d/R_d = 0.2$. The coldness of the disc is controlled by the central radial velocity dispersion which we assume to be $\sigma_{R0} = 10$ km s^{-1}. This translates to the Toomre parameter $Q = 3.82$ at $R = 2.5R_d$ and guarantees that our dwarf is stable against formation of the bar in isolation for the time-scales of interest here. We verified this by evolving the dwarf galaxy in isolation for 10 Gyr.

The host galaxy was chosen to resemble the model MWb of Widrow & Dubinski (2005). It had a dark matter halo of mass $M_H = 7.7 \times 10^{11}$ M$_\odot$ and concentration $c = 27$. The disc of the host had a mass $M_D = 3.4 \times 10^{10}$ M$_\odot$, the scalelength $R_D = 2.82$ kpc and thickness $z_D = 0.44$ kpc. The central radial velocity dispersion of the disc was $\sigma_{R0} = 121$ km s^{-1} which corresponds to the Toomre parameter $Q = 2.2$ again making the disc stable against bar formation for time-scales of interest.

Although there is evidence that the Milky Way has a bar (e.g. Blitz & Spergel 1991; Dwek et al. 1995; Martinez-Valpuesta & Gerhard 2011; Romero-Gómez et al. 2011), we specifically chose a model for the host galaxy that does not form a bar since this makes the host potential constant in time. The main reason for this choice is that we are most interested here in modelling the effect of the tidal forces on the growth and evolution of the bar in the dwarf. The presence of a time-dependent bar in the Milky Way-like host would induce a second time dependence whose influence would be difficult to disentangle from the tidal effects. Furthermore, both observational (e.g. Stanek et al. 1997) and theoretical (e.g. Shen et al. 2010) studies indicate that the bar in the Milky Way is not very strong. Moreover, its half-length is of the order of 4 kpc, i.e. much smaller than our adopted pericentre distance. It is thus unlikely to significantly influence the evolution of the tidal bar in the dwarf. For simplicity, we also neglect other components of the Milky Way structure such as the bulge, the stellar halo, the distinction into thin/thick disc etc. The mass of these components is at least a few

times smaller than the disc mass we assume and probably of the order of the uncertainty of the mass distribution in the two main components (Widrow & Dubinski 2005).

We placed the dwarf galaxy initially at an apocentre of a typical, eccentric orbit around the Milky Way with apo- to pericentre distance ratio of $r_{apo}/r_{peri} = 120/25$ kpc. Due to a rather small mass of the dwarf the orbit decays only a little in time as a result of dynamical friction. The dwarf's disc, the disc of the Milky Way and the orbit were initially all coplanar and the dwarf's disc was in prograde rotation with respect to the orbit. This configuration, together with the stability of the Milky Way's disc, makes sure that the tidal forces experienced by the dwarf during the evolution are only controlled by the dwarf's distance from the host galaxy and not by other subtle changes of the potential.

The evolution of the dwarf was followed for 10 Gyr using the GADGET-2 *N*-body code (Springel, Yoshida & White 2001; Springel 2005) and we saved 201 simulation outputs, one every 0.05 Gyr (which is significantly smaller than the dynamical time of stars in the dwarf's disc). The code configuration was that of Newtonian space with vacuum boundary conditions and the gravity calculations were done with a tree option. We adopted the softening scales of $\epsilon_d = 0.02$ kpc and $\epsilon_h = 0.06$ kpc for the disc and halo of the dwarf and $\epsilon_D = 0.05$ kpc and $\epsilon_H = 2$ kpc for the disc and halo of the Milky Way, respectively. These choices were informed by the study of Power et al. (2003) and allow us to avoid strong discreteness and two-body effects in the case of systems of given characteristic scales and particle numbers.

3 OVERVIEW OF THE EVOLUTION

The repeated action of the tidal force from the Milky Way made the dwarf galaxy evolve as envisioned by the tidal stirring scenario originally proposed by Mayer et al. (2001) and studied in more detail by Klimentowski et al. (2009), Kazantzidis et al. (2011) and Łokas et al. (2011, 2012). The main signatures of such evolution involve the mass loss, the morphological transformation of the stellar component and the changes in the kinematics of the stars. Since we are interested here in the formation and evolution of the bar, we focus on the latter two. In order to give an idea of the overall evolution of the dwarf, we first perform rough measurements of the main, global features.

Inspection of the final state of the dwarf reveals that, in spite of the strong mass-loss, it still possesses a well visible bound stellar component of radius of the order of 1 kpc. Therefore, we may measure the properties of the dwarf at all times using stars within some fixed radius comparable to this value, or smaller. One could choose to measure the dwarf's properties at some characteristic scale such as the radius where maximum circular velocity occurs (as was done in Klimentowski et al. 2009 and Kazantzidis et al. 2011), the half-light radius (Łokas et al. 2011, 2012) or the break radius (where the transition to the tidal tails occurs, see e.g. Łokas, Gajda & Kazantzidis 2013). However, the caveat of such measurements is that such radii also evolve in time and the interpretation of the results may not be straightforward.

For each simulation output, we determine the centre of the dwarf galaxy by calculating the centre of mass of the stars iteratively in decreasing radii until convergence is reached. We start the analysis of the properties of the dwarf galaxy by measuring the mass of stars and dark matter within a fixed radius r_m from the centre of the dwarf equal to 1 and 0.5 kpc. The results are shown in the upper (stars) and middle (dark matter) panel of Fig. 1 with the red curve corresponding to measurements within $r_m = 0.5$ kpc
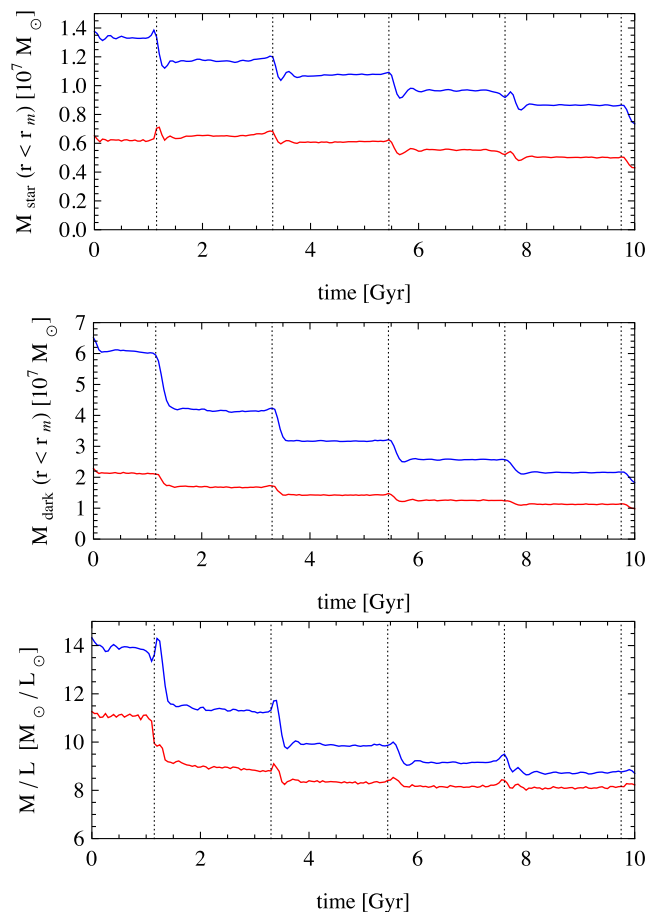

Figure 1. The evolution of the mass of the dwarf galaxy. The upper panel shows measurements of the mass of stars, the middle panel the mass of the dark matter component and the lower one the mass-to-light ratio (assuming $M/L = 2.5$ M$_\odot$/L$_\odot$ for the stars) within a fixed maximum radius r_m. In each panel, the red curve corresponds to measurements within $r_m = 0.5$ kpc and the blue one within $r_m = 1$ kpc. Vertical dotted lines indicate pericentre passages.

and the blue one within $r_m = 1$ kpc. In the lower panel of the figure, we also plot the mass-to-light ratio within these radii assuming $M/L = 2.5$ M$_\odot$/L$_\odot$ for the stars. The results show that mass in both components is systematically lost from within both limiting radii, except for the period after the first pericentre passage where the stellar content within 0.5 kpc is not diminished. The mass-to-light ratio systematically decreases to converge to about (8–9) M$_\odot$/L$_\odot$ at the end of the evolution. This means that dark matter is stripped more efficiently than stars and that the stripping affects even the inner part of the dwarf where the measurements were done.

To make sure we include a sufficient number of stars from the main body of the dwarf and at the same time avoid the contamination from the tidal tails for all the following measurements discussed in this section we fix the maximum radius at $r_m = 0.5$ kpc. We note that the results of the measurements do not depend strongly on this choice. Thus, for each output we select stars within r_m, find the principal axes of the stellar component from the tensor of inertia and rotate the stellar positions and velocities to align them with the principal axes. In the following, we will always refer to the major, intermediate and minor axis of the stellar component as *x*, *y* and *z* respectively and the corresponding axis lengths as *a*, *b* and
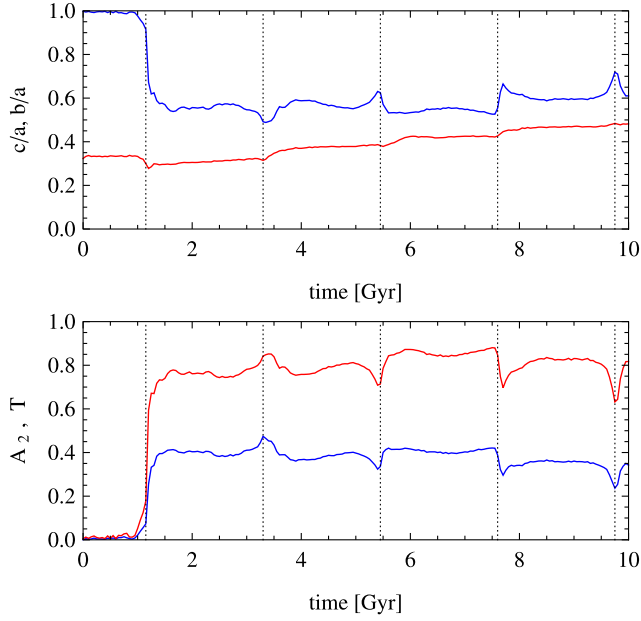
Figure 2. The evolution of the shape of the stellar component of the dwarf galaxy. The upper panel shows the evolution of the axis ratios c/a (red lower line) and b/a (blue upper line) in time. The lower panel shows the evolution of the bar mode A_2 (blue lower line) and the triaxiality parameter T (red upper line) in time. All measurements were performed for stars within a constant radius of 0.5 kpc. Vertical dotted lines indicate pericentre passages.

c. Having aligned the stellar distribution in this way, we estimated the axis ratios as a function of time. The results in terms of c/a and b/a are shown in the upper panel of Fig. 2 as the red and blue line, respectively. At the first pericentre passage the b/a value drops significantly from the initial $b/a = 1$ characteristic of the disc, while c/a stays roughly at the same level. This means that the initial disc transforms into a triaxial stellar component. This triaxial shape is maintained until the end of the simulation, although both b/a and c/a increase.

The properties of the shape are further illustrated in the lower panel of Fig. 2 where the red line shows the triaxiality parameter $T = [1 - (b/a)^2]/[1 - (c/a)^2]$. The values of the parameter $0 < T < 1/3$ indicate the oblate shape, the values $1/3 < T < 2/3$ a triaxial shape and $2/3 < T < 1$ a prolate shape. With $T > 0.7$ almost at all outputs after the first pericentre, we conclude that the shape of the stellar component is decidedly prolate. This strongly suggests that at the first pericentre passage, the stellar component of the dwarf formed a bar. To confirm this statement, we also measured the bar mode A_2 from the positions of the stars projected on to the xy plane (along the shortest axis). In general, the amplitude of the mth Fourier mode of the discrete distribution of stars in the simulated galaxy is calculated as $A_m = (1/N) \left| \Sigma_{j=1}^{N} \exp(im\phi_j) \right|$, where ϕ_j are the particle phases in cylindrical coordinates and N is the total number of stars (Sellwood & Athanassoula 1986; Debattista & Sellwood 2000). The value of the bar mode $m = 2$ is shown with the second (blue) line in the lower panel of Fig. 2. As values of A_2 are above 0.2 at all times after the first pericentre, we conclude that indeed a bar is formed at this time and this shape persists until the end of the simulation.

This conclusion is further supported by the measurements of the kinematic properties of the stellar component. The kinematic measurements were performed using a system of spherical coordinates such that at every simulation output the angle θ measures the an-
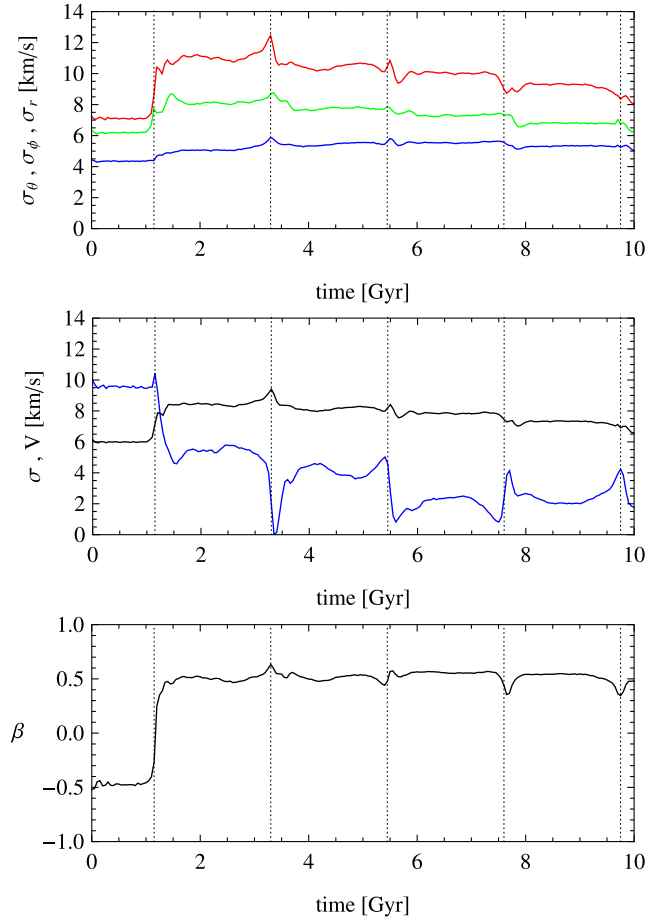

Figure 3. The evolution of the kinematics of the stellar component of the dwarf galaxy. Upper panel: the evolution of the velocity dispersions of the stars in spherical coordinates σ_r (red upper line), σ_ϕ (green middle line) and σ_θ (blue lower line). Middle panel: the evolution of the averaged 1D velocity dispersion σ (black line) and the rotation velocity V (blue line). Lower panel: evolution of the anisotropy parameter β. All measurements were performed for stars within a constant radius of 0.5 kpc. Vertical dotted lines indicate pericentre passages.

gular distance from the shortest axis (z) of the stellar component, while ϕ is measured in the xy plane. In the upper panel of Fig. 3, we plot the velocity dispersions of the stars in the three coordinates. The three lines from the top to the bottom correspond to σ_r (red), σ_ϕ (green) and σ_θ (blue) respectively. At the first pericentre passage all dispersions increase, signifying the transition from the overall streaming motion of the stars (rotation) to the random motions manifesting themselves via the velocity dispersion. However, the radial dispersion increases most as expected in the case of the formation of a bar which is supported by more radial orbits. Later on, the dispersions decrease due to mass-loss, except for σ_θ which remains roughly constant as a result of the thickening of the stellar component in time.

The middle panel of Fig. 3 shows the overall contribution of random versus ordered motion in terms of a 1D velocity dispersion $\sigma = [(\sigma_r^2 + \sigma_\phi^2 + \sigma_\theta^2)/3]^{1/2}$ (black line) and the mean velocity (blue line) around the shortest axis (along the ϕ coordinate of the spherical system, $V = V_\phi$) i.e. the rotation velocity. The overall trend is for the rotation to decrease (especially at the first pericentre passage) and the dispersion to remain roughly constant in time or slightly decrease due to mass-loss. The transition from mostly circular orbits
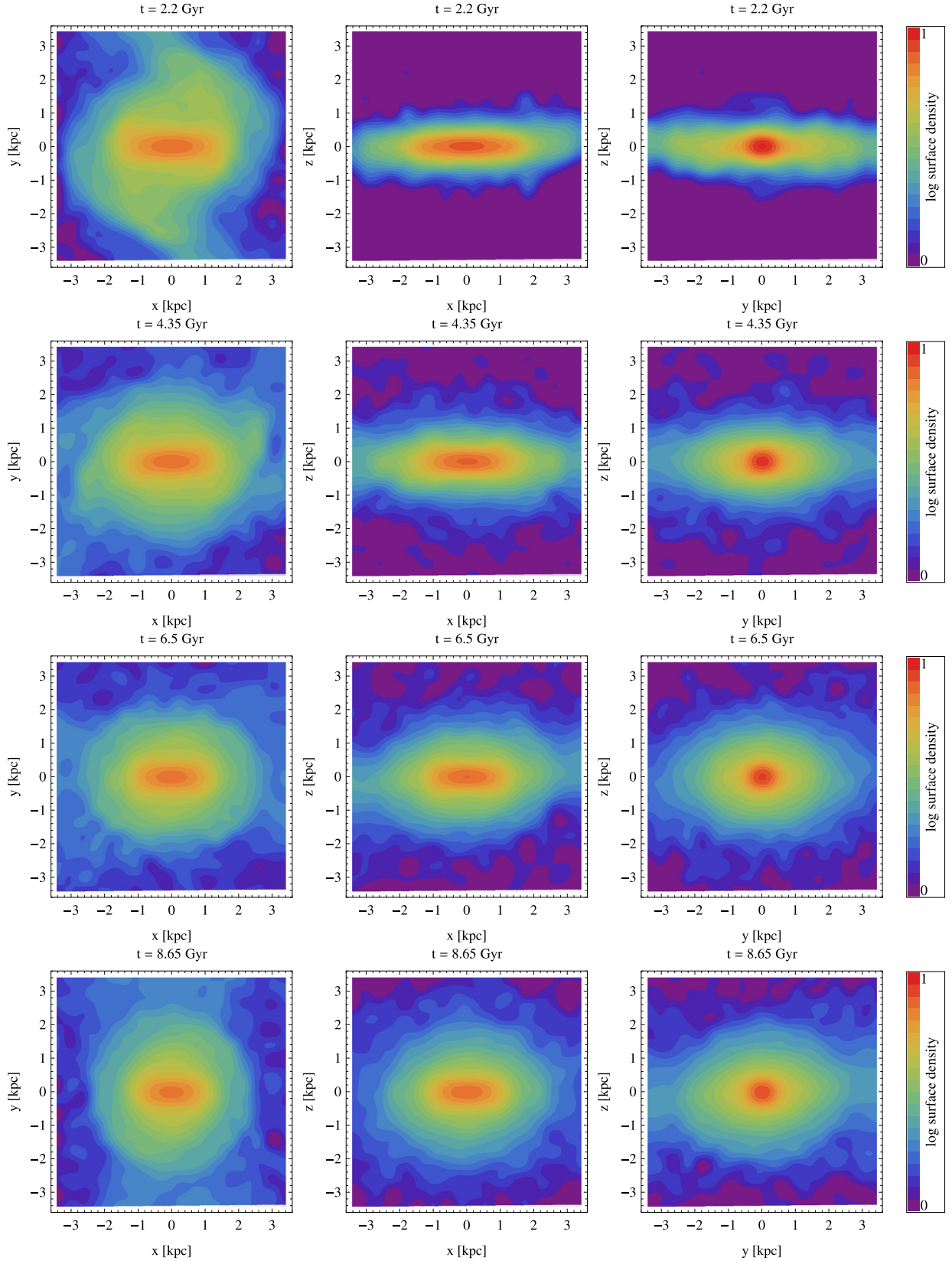
Figure 4. Surface density distributions of the stars in the dwarf at subsequent apocentres at $t = 2.2, 4.35, 6.5, 8.65$ Gyr (rows) and along different lines of sight: the shortest (z), intermediate (y) and longest (x) axis of the stellar component (columns, from left to right). The surface density measurements were normalized to the maximum value $\Sigma_{max} = 9.8 \times 10^5$ stars kpc^{-2} occurring for the line of sight along the x-axis at $t = 2.2$ Gyr. Contours are equally spaced in log Σ with Δlog $\Sigma = 0.05$.

Figure 5. The bar mode A_2 as a function of cylindrical radius R. The upper panel shows the measurements at subsequent apocentres and the lower panel at subsequent pericentres. At apocentres, the bar mode curves show a characteristic shape with a maximum, while at pericentres they are monotonically increasing.

Figure 6. The even modes A_m as a function of cylindrical radius R. The upper panel shows the profiles of the first four even modes at the second apocentre ($t = 2.2$ Gyr) and the lower panel the analogous measurements at the first pericentre passage ($t = 1.2$ Gyr). The modes all have a similar shape and preserve the hierarchy with the lower order modes having always higher values.

of the stars (in the initial disc) to more radial orbits in the bar is also very well visible in the evolution of the anisotropy parameter of the stars $\beta = 1 - (\sigma_\theta^2 + \sigma_\phi'^2)/(2\sigma_r^2)$, where the second velocity moment $\sigma_\phi'^2 = \sigma_\phi^2 + V_\phi^2$ includes rotation. The dependence of β on time is shown in the lowest panel of Fig. 3. Clearly, the circular orbits of stars ($\beta < 0$) in the initial disc are replaced after the first pericentre by more radial orbits ($\beta > 0$) which survive until the end of the simulation.

Fig. 4 shows the surface density distributions of the stars in the dwarf at subsequent apocentres of the orbit (from the second at $t = 2.2$ Gyr to the fifth at $t = 8.65$ Gyr). The rows of the figure correspond to the different times of the simulation, while the columns to different lines of sight: along the shortest (z, face-on), intermediate (y, side-on) and longest (x, end-on) axis of the stellar distribution (as determined from stars within 0.5 kpc). In the left-hand and mid-
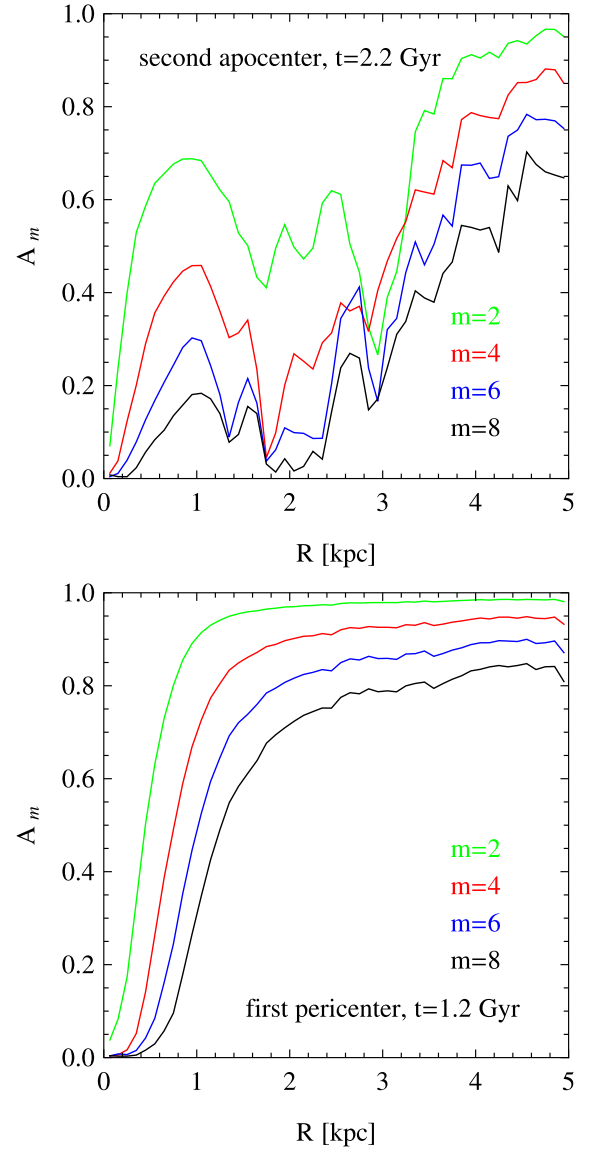
dle column the line of sight is perpendicular to the bar and the bar is clearly visible. At the second apocentre (at $t = 2.2$ Gyr), the stellar component of the dwarf is still restricted to the initial plane of the disc. At later times, the stellar component becomes thicker and at the final apocentre the outer density contours are almost spherical while the bar-like shape is only preserved in the central part of the dwarf.

4 THE STRENGTH OF THE BAR

In the previous section, we measured the global properties of the dwarf galaxy as a function of time, finding convincing evidence for the formation of a bar after the first pericentre. The strength of the bar can be quantified in more detail by measuring the profile of the bar mode A_2 as a function of a cylindrical radius R. The coordinate
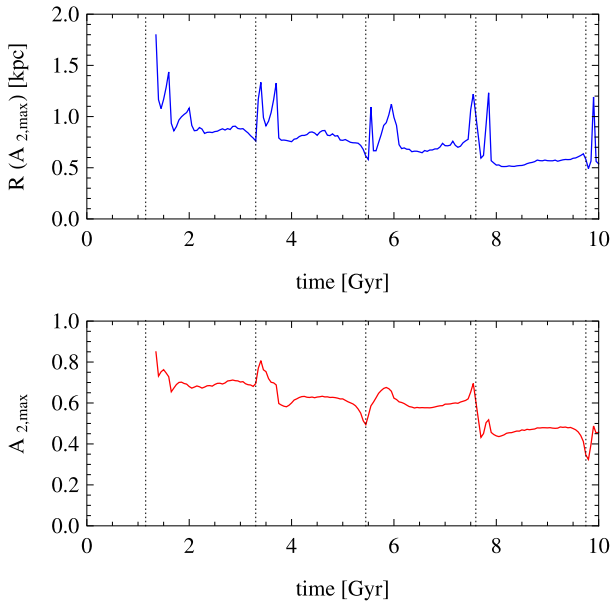
Figure 7. The radius at which the first maximum of the bar mode $A_{2,\,max}$ occurs (upper panel) and the value of the maximum of the bar mode $A_{2,\,max}$ (lower panel) as a function of time. Vertical dotted lines indicate pericentre passages.

system for these measurements was chosen so that R is in the disc equatorial plane (xy) as determined previously from the principal axes of the stellar component within 0.5 kpc.

The measurements of the values of the bar mode as a function of R are shown in Fig. 5 at subsequent apocentres (upper panel) and pericentres (lower panel). At pericentres, the dwarf is stretched by tidal forces from the Milky Way so that the bar mode increases monotonically with radius. At apocentres, when the dwarf recovers its equilibrium, the bar mode displays a characteristic shape, growing with radius up to a maximum value and then decreasing. After reaching a minimum value, A_2 increases again as we transit from the bound component of the dwarf to the tidal tails. The tidal tails are symmetrical elongated features on both sides of the dwarf (see e.g. Łokas et al. 2013) which obviously results in the A_2 approaching unity at large radii. The maximum value of the A_2 mode decreases with time which means that the bar becomes weaker as the evolution proceeds, a feature that was not obvious from the global single-value measurement of A_2 shown in the lower panel of Fig. 2.

It is also instructive to look at the higher order Fourier modes of the distribution of the stars. Fig. 6 compares the profiles of the non-zero even modes with $m = 2, 4, 6, 8$ at the second apocentre (upper panel) and the first pericentre (lower panel). We note that the odd modes (not shown) all have very low amplitudes within the main body of the dwarf which means that the distribution of the stars is symmetrical. The measurements of even modes show that while the $m > 2$ even modes are systematically lower than the most significant $m = 2$ bar mode and preserve the hierarchy at all times, they nevertheless assume values decidedly different from zero. This means that the density distribution in the tidally induced bar in our simulation cannot be described by the $m = 2$ alone but higher even order components are not negligible. Interestingly, the same behaviour was seen in simulated galaxies forming bars in isolation by Athanassoula & Misiriotis (2002, their fig. 7) and by Ohta, Hamabe & Wakamatsu (1990) who studied surface photometry of
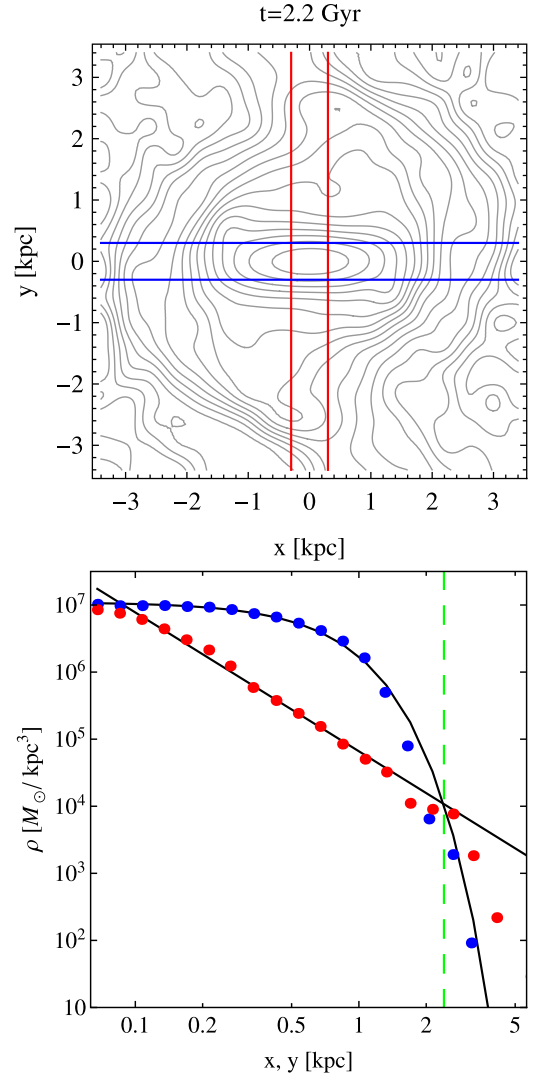

Figure 8. Upper panel: an example of the measurement of the density profiles at the second apocentre ($t = 2.2$ Gyr). The contours indicate the levels of equal surface density distribution of the stars with the bar clearly visible along the x-axis. The measurements are done by counting stars in cylinders of radius 0.3 kpc in bins spaced equally in log x (along the bar, blue lines) and y (perpendicular to the bar, red lines). Lower panel: density profiles measured for the output shown in the upper panel. The blue (red) dots indicate measurements along (perpendicular to) the bar. Solid black lines show the analytic fits to the measured profiles. The vertical green dashed line indicates the radius where the two fitted profiles are equal, adopted as the measure of the length of the bar.

six real barred spirals (see their fig. 4). Such a hierarchy of modes thus seems to be a general feature of barred galaxies, independent of their size and of the way they formed.

We adopt the maximum value of the bar mode $A_{2,\,max}$ as the measure of the strength of the bar. Fig. 7 shows in the upper panel the cylindrical radius R at which the first maximum of the bar mode occurs as a function of time. The measurements are only significant between pericentres since near pericentres the profile of A_2 is increasing and there is no well-defined maximum (see Fig. 5). The lower panel of the figure plots the value of the maximum bar mode $A_{2,\,max}$ as a function of time. These detailed measurements confirm the impression from Fig. 5: in the long run the maximum of the bar mode decreases from about 0.7 after the first pericentre
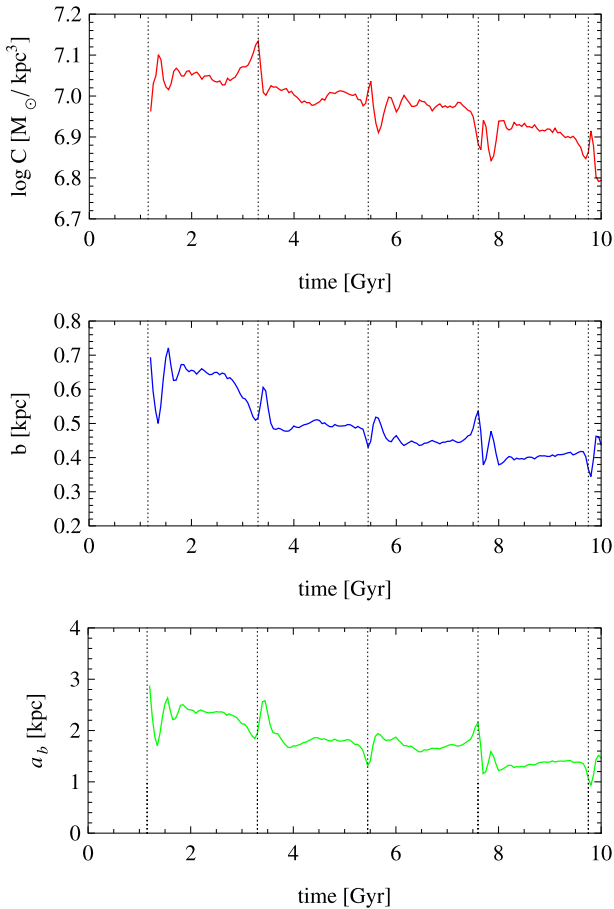
Figure 9. The upper and middle panels show the parameters of the formula $\rho_1(x) = C \exp[-(x/b)^{3/2}]$ fitted to the measured density profiles along the bar as a function of time: the normalization C and the scalelength b. The lower panel plots the length of the bar a_b defined as the radius where the fitted density profiles along the bar and perpendicular to it converge. Vertical dotted lines indicate pericentre passages.

to about 0.45 after the fourth one. Thus, we conclude that the bar becomes weaker in time and the changes in the bar strength are most significant at pericentres while between them $A_{2,\,max}$ remains roughly constant.

5 THE LENGTH OF THE BAR

Athanassoula & Misiriotis (2002) discussed different ways to measure the bar length. In principle, the profiles of A_2 such as those shown in Fig. 5 could be used to determine the length of the bar. Such a procedure works in general for simulated bars forming in isolated disc galaxies as in such cases the profile of A_2 declines smoothly after reaching the maximum value. One can then find, e.g. the radius where A_2 drops to some fraction (e.g. 1/2) of the maximum value and use this scale as the measure of the bar length. In our case, however, the profile does not always drop sufficiently before it starts to increase again due to the transition to the tidal tails. One solution would be to find a minimum of A_2 and adopt the corresponding scale as the length of the bar. However, even after smoothing our A_2 profiles are rather noisy and such measurements result in very imprecise estimates of the bar length.

We therefore measured the length of the bar using a different approach, similar to method (v) discussed by Athanassoula &
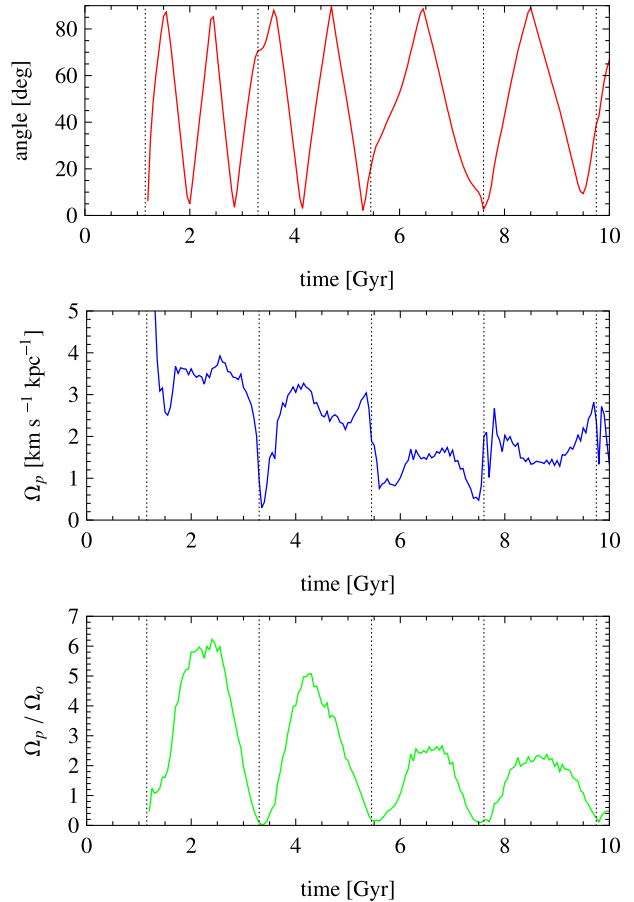
Figure 10. Upper panel: the angle between the nearest side of the bar's major axis and a fixed axis of the simulation box as a function of time. Middle panel: the pattern speed of the bar as a function of time. Lower panel: the ratio of the bar's pattern speed to the angular velocity of the dwarf on the orbit. Vertical dotted lines indicate pericentre passages.

Misiriotis (2002, section 8). Namely, we calculated the density of stars along the bar major axis (i.e. along the x-axis of the stellar component) and perpendicular to it (along the y-axis) in cylinders of radius 0.3 kpc and logarithmic bins in x and y. An example of such measurements after $t = 2.2$ Gyr from the start of the simulation (second apocentre) is shown in the upper panel of Fig. 8. The contours indicate equal levels of surface density of stars similar to those plotted in Fig. 4 with the bar well visible along the x-axis in the inner part of the picture. The cylinders of stars selected for the measurements are indicated with blue (along the bar) and red (perpendicular to the bar) lines. The measured density profiles are plotted as dots of the corresponding colours in the lower panel of Fig. 8. As expected, the measurement along the bar (blue points) is rather flat in the centre, reflecting the approximately constant density distribution of the stars in the bar. The difference between the densities measured in the two directions first grows with radius and then the two converge. We will adopt the scale where the two densities converge as the measurement of the length of the bar.

In order to avoid the noise due to the limited number of stars in the outer bins, we fitted the profiles with analytic functions. We find that the density along the bar is well approximated at all times by an exponential $\rho_1(x) = C \exp[-(x/b)^{3/2}]$ where C is the normalization constant and b is the characteristic scalelength. The density distribution perpendicular to the bar is well approximated
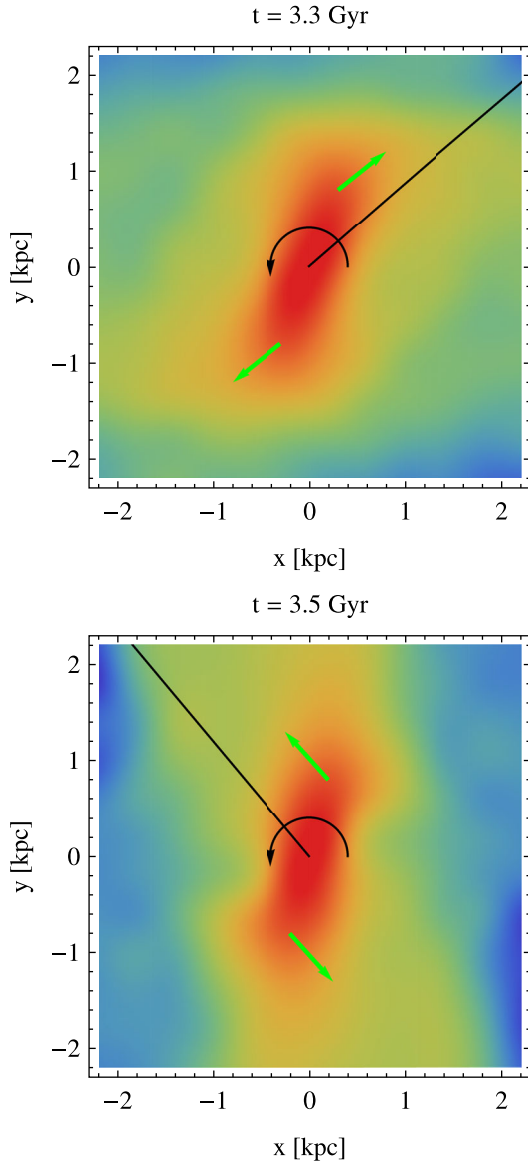
Figure 11. The change of direction of tidal torque from the Milky Way near the second pericentre passage. Plots show the surface distribution of the stars in the dwarf projected on to the orbital plane at $t = 3.3$ (upper panel) and $t = 3.5$ Gyr (lower panel). The colour coding is similar as in Fig. 4 but normalized to the central density value for this stage and line of sight $\Sigma_{max} = 6.8 \times 10^5$ stars kpc^{-2}. In both panels the curved arrows in the centre indicate the direction of rotation of the bar. The solid lines show the direction towards the Milky Way. Green arrows indicate the tidal forces acting on the bar. Between the outputs the direction of the tidal torque changes from one slowing down the bar to one speeding it up.

by a simple power law $\rho_2(y) = Dy^{-d}$. For every simulation output we measured the density profiles in this way and fitted the formulae to the measurements. The fitted values of the C and b parameters of the density distribution along the bar are especially interesting and their evolution is shown as a function of time in the upper and middle panel of Fig. 9. We see that the values of both parameters decrease in time reflecting the stripping of the stars (decrease of normalization) and shortening of the bar (decrease of scalelength). The parameters of the power-law fit $\rho_2(y)$ do not show any clear trend in time. Both the normalization D and the power-law index d stay roughly constant in time with d in the range of 2–2.5. We
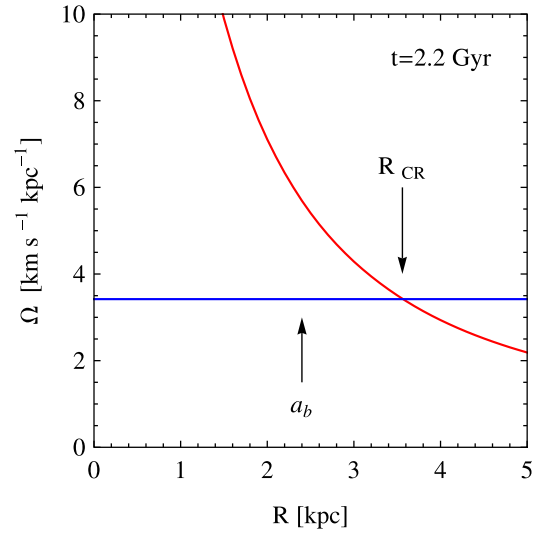

Figure 12. The circular frequency of the dwarf galaxy as a function of radius (red line) in comparison with the pattern speed of the bar Ω_p (blue line) at the second apocentre ($t = 2.2$ Gyr). These two quantities are equal at the corotation radius $R_{CR} = 3.6$ kpc marked with a black arrow. The second black arrow indicates the length of the bar at this time $a_b = 2.4$ kpc. The ratio of the two $s = R_{CR}/a_b = 1.5$ is close to unity, so the bar is rather fast.

note that the particular choice of the fitting formulae does not have to apply to other kinds of bars. We used them mainly as a tool to smooth the results of bar length measurements and because the formulae were general enough to accommodate the density profiles of our bar at all times.

Solving $\rho_1(x) = \rho_2(y)$ with the fitted parameters, we find for each simulation output the scale at which both density profiles converge. The scale, which we identify with the length of the bar, a_b, is plotted as a function of time in the lower panel of Fig. 9. The length of the bar thus decreases during the evolution from $a_b = 2.4$ kpc after the first pericentre to $a_b = 1.3$ kpc after the fourth. Note that the decrease of the bar length occurs mainly at pericentre passages so it is due to tidal shocking and not due to secular evolution since between pericentres the length remains approximately constant in time.

6 THE PATTERN SPEED OF THE BAR

We finally also look at the pattern speed of the bar. The simplest way to visualize its variability is to measure the angle between the major axis of the stellar component and a fixed axis of the simulation box. For this measurement, we use the orientation of the major axis determined as before using stars within a constant radius of 0.5 kpc. The angle between the major axis of the bar and a fixed axis in the initial orbital plane of the dwarf is shown as a function of time in the upper panel of Fig. 10. At each output, we calculated the angle between the fixed axis and the nearest part of the bar, which is why the angle is always in the range between 0 and 90 deg. The measurements start after the first pericentre when the bar is formed. The bar lies almost exactly in the orbital plane of the dwarf at all times as indicated by the values of the angle covering the whole range of 0–90 deg. The tumbling of the bar seems much slower in the second half of the evolution (after the third pericentre passage), as shown by the much slower changes of the angle.

The actual pattern speed calculated as a change between the directions of the bar's major axis in subsequent simulation outputs

is plotted in the middle panel of Fig. 10. The pattern speed decreases in the long run but shows a rather strong variability, mostly, but not only, at the pericentre passages. We note that the variability of the pattern speed mirrors closely our measurements of the mean rotation velocity of the stars discussed in Section 3 (see the blue line in the middle panel of Fig. 3). This means that after the first pericentre the rotation is mostly due to the tumbling of the bar.

A particularly interesting behaviour occurs at the second pericentre passage when the pattern speed drops almost to zero, i.e. the bar almost stops rotating but then speeds up again. The variation of the pattern speed at this moment (and its general evolution) can be understood by referring to Fig. 11 where we show the orientation of the bar with respect to the direction towards the centre of the Milky Way. The upper and lower panel show respectively the projections of the stellar component on to the orbital plane at $t = 3.3$ and 3.5 Gyr, that is just before and just after the second pericentre. The circular arrow in the centre marks the anticlockwise direction of the bar's rotation. In each panel, the solid black line indicates the direction towards the Milky Way and the two green arrows show the direction of tidal forces acting on the two sides of the bar. At the earlier time depicted in the figure (upper panel), the torque due to the tidal forces is directed so that it slows the bar. At the later time (lower panel), the orientation of the bar with respect to the direction to the Milky Way changes and the torque now speeds up the bar. The result is for the bar to regain the pattern speed up to almost the same level as before the pericentre.

The subsequent changes of the pattern speed, the more violent ones at pericentres, as well as the milder ones between pericentres can all be traced to a particular orientation of the bar with respect to the tidal force acting at a given time. In particular, at the third pericentre passage the bar is systematically slowed down (the orientation is similar as in the upper panel of Fig. 11), while at the fourth pericentre the bar is continuously accelerated (the orientation is similar as in the lower panel of Fig. 11).

It is also interesting to compare the pattern speed of the bar Ω_p to the angular velocity of the dwarf galaxy on its orbit Ω_o. The ratio of the two quantities is plotted in the lower panel of Fig. 10. At pericentres, the dwarf obviously moves very fast on its rather eccentric orbit so the ratio Ω_p/Ω_o is close to zero. Between pericentres, the ratio increases up to a factor of a few and at apocentres is never below two. Note that $\Omega_p/\Omega_o = 1$ would mean that the bar is tidally locked as the Moon is locked to the Earth and only one and always the same side of the bar would be directed towards the Milky Way. This is clearly not the case. However, an interesting evolutionary stage takes place near the fourth apocentre of the orbit ($t = 6$–7 Gyr) when $\Omega_p/\Omega_o \approx 5/2$ and the angle between the bar and the direction to the Milky Way stays in the range of 0–20 deg. This points to a possibility of a 5/2 resonance between the rotational and orbital motion of the bar, similar to the 3/2 resonance of Mercury around the Sun (Correia & Laskar 2004).

Finally, we estimate the speed of the bar in terms of the quantity $s = R_{CR}/a_b$ where R_{CR} is the corotation radius (where the circular frequency of the dwarf galaxy Ω equals the pattern speed Ω_p) and a_b is the length of the bar estimated in the previous section. According to theory of bars (Binney & Tremaine 2008), they can only exist at radii $R < R_{CR}$ so all bars have $s > 1$ and are classified as fast if $s \approx 1$ or slow when $s \gg 1$. We calculated the corotation radii for a number of outputs and compared them with corresponding bar lengths. An example of such a comparison for the second apocentre ($t = 2.2$ Gyr) is shown in Fig. 12. The red line is the circular frequency of the dwarf galaxy $\Omega = [GM(r)/r^3]^{1/2}$ as a function of radius (calculated with radial step of 0.1 kpc) and the blue line is the

Table 1. Estimates of the speed of the bar at subsequent apocentres.

Apocentre	Time (Gyr)	R_{CR} (kpc)	a_b (kpc)	R_{CR}/a_b
2	2.2	3.6	2.4	1.5
3	4.35	3.4	1.8	1.9
4	6.5	4.7	1.6	3.0
5	8.65	4.4	1.3	3.3

pattern speed from the middle panel of Fig. 10. The two are equal at $R_{CR} = 3.6$ kpc while the bar length at this time is $a_b = 2.4$ kpc (see the lower panel of Fig. 9). This gives us $s = 1.5$, a value not very different from unity, thus the bar at this stage may be classified as fast.

Similar calculations at all apocentres give the results listed in Table 1. We restricted ourselves to the measurements at apocentres because near pericentres the pattern speed varies strongly and in particular can be very low which leads to high and thus meaningless estimates of the corotation radius. We see that at subsequent apocentres the values of s systematically increase, up to $s = 3.3$ at the last apocentre, so the bar becomes slower with time. This result is not obvious at first sight because R_{CR} and a_b behave differently in time. While the bar length a_b decreases monotonically between apocentres (see Table 1), the R_{CR} increases or decreases with time. The latter is itself a combination of the circular frequency, which decreases monotonically with time as a result of mass-loss, and the pattern speed, which does not have an obvious monotonic behaviour. The overall measure of the bar speed in terms of R_{CR}/a_b confirms however the general impression from the behaviour of the much simpler quantity such as the mean rotation velocity (see the middle panel of Fig. 3) or the mean angular momentum which behaves in a way very similar to the rotation velocity.

The main physical reason for the slowdown of the bar over large time-scales can be traced to the effect of tidal stripping of the stars which happens preferentially to stars on prograde orbits (as is the case in our simulation) due to resonances between the orbital and intrinsic motion of the stars (D'Onghia et al. 2010). The stripped stars feed the tidal tails of the dwarf galaxy and move on their own orbits around the Milky Way. Thus, the angular momentum of the stars is taken by the stripped stars and not transferred to the dark matter particles of the dwarf's halo as the angular momentum of the halo does not significantly change during the evolution.

7 DISCUSSION

We studied the formation and evolution of a stellar bar induced in a discy dwarf galaxy orbiting the Milky Way by tidal forces from the host. We measured the main properties of the bar such as its strength, length and pattern speed as a function of time and related the pattern speed to the dwarf's circular frequency. The comparison between the two quantities led us to conclude that while the bar is quite fast at its birth after the first pericentre passage, it becomes slower with time. This has important consequences for understanding the process of formation of dSph galaxies of the Local Group.

As the tidal evolution proceeds, the bar becomes shorter and thicker and the stellar component changes its shape towards spherical. One could attempt to explain the shortening of the bar as due to the mass-loss that results in decreasing the circular frequency of the dwarf. If the pattern speed of the bar remained constant in time, the corotation radius would also decrease. Since the bar

cannot extend beyond the corotation radius, this would explain why it becomes shorter and thus relate the mass-loss to the morphological transformation. The actual behaviour, however, turns out to be more complicated. As we demonstrated in the previous sections, the pattern speed of the bar is not constant but subject to abrupt changes near pericentres and more benign ones in the other parts of the orbit, depending on the orientation of the bar major axis with respect to the direction of the tidal force. This causes the corotation radius to vary non-monotonically with time. There is thus no simple relation between the length of the bar and the corotation radius. The bar seems to become shorter just due to randomization of stellar orbits resulting from tidal shocking.

It seems to be generally believed that a common intermediate stage of the evolution of discy dwarfs towards a more spherical shape is that of bar buckling. Buckling seemed to occur in a large fraction of the cases of tidally induced bars studied by Mayer et al. (2001). They claimed that buckling contributes to the heating of the disc even more than the tidal heating itself. The occurrence of buckling is usually accompanied by an increase of the ratio of velocity dispersions along the shortest axis and in the bar plane σ_z/σ_R and by non-zero amplitude of the odd Fourier mode A_1 in the edge-on view (e.g. Martinez-Valpuesta et al. 2006). We have looked for signatures of bending instabilities in our bar by measuring the ratio σ_z/σ_R as a function of time (for stars within radius of 1 kpc). This ratio is close to 0.4 after the first pericentre when the bar forms and increases steadily with time to about 0.6 at the end of the evolution. There is no abrupt increase of σ_z/σ_R that would signify the presence of buckling. We have also measured the A_1 mode for the stars seen along the intermediate axis (as in the middle column of Fig. 4) and did not find it significantly different from zero.

The actual presence of buckling was only detected by visual inspection of surface density maps such as those in Fig. 4. Slight asymmetries in the distribution of stars with respect to the bar plane in the edge-on view were observed for a brief period between 3.5 and 3.8 Gyr from the start of the simulation, that is soon after the second pericentre passage. As expected, the occurrence of buckling was accompanied by the decrease in the bar strength (A_2 and $A_{2,\,max}$) seen in the lower panels of Figs 2 and 7 at these times. This brief period of buckling instability was followed by the formation of the boxy/peanut shape visible in the edge-on view of the surface distribution of stars at $t = 4.35$ Gyr in Fig. 4.

In this paper, we explored the properties of the tidally induced bar only in one initial and rather special configuration, that of coplanar discs of the dwarf and the host galaxy and the dwarf's disc rotation exactly prograde with respect to the orbital motion. While the orientation of the Milky Way disc with respect to the orbital plane of the dwarf seems of little consequence, the angle between the dwarf disc's angular momentum and the orbital angular momentum has dramatic consequences. Preliminary simulations show that if the dwarf disc orientation is exactly retrograde the bar does not form at all and the dwarf's stellar component remains discy. For intermediate orientations, the bar does form but it is typically weaker than in the case studied here. The dependence of the properties of tidally induced bars on this and other parameters will be discussed in follow-up papers.

ACKNOWLEDGEMENTS

REFERENCES

Athanassoula E., 2002, ApJ, 569, L83
Athanassoula E., 2003, MNRAS, 341, 1179
Athanassoula E., 2005, MNRAS, 358, 1477
Athanassoula E., 2013, in Falcón-Barroso J., Knapen J. H., eds, Secular Evolution of Galaxies. Cambridge Univ. Press, Cambridge, p. 305
Athanassoula E., Misiriotis A., 2002, MNRAS, 330, 35
Athanassoula E., Sellwood J. A., 1986, MNRAS, 221, 213
Athanassoula E., Machado R. E. G., Rodionov S. A., 2013, MNRAS, 429, 1949
Besla G., Kallivayalil N., Hernquist L., Robertson B., Cox T. J., van der Marel R. P., Alcock C., 2007, ApJ, 668, 949
Binney J., 1978, MNRAS, 183, 779
Binney J., Tremaine S., 2008, Galactic Dynamics: Second Edition. Princeton Univ. Press, Princeton, NJ
Blitz L., Spergel D. N., 1991, ApJ, 379, 631
Cheung E. et al., 2013, ApJ, 779, 162
Coleman M. G. et al., 2007, ApJ, 668, L43
Combes F., Debbasch F., Friedli D., Pfenniger D., 1990, A&A, 233, 82
Correia A. C. M., Laskar J., 2004, Nature, 429, 848
D'Onghia E., Vogelsberger M., Faucher-Giguere C.-A., Hernquist L., 2010, ApJ, 725, 353
Debattista V. P., Sellwood J. A., 2000, ApJ, 543, 704
Dubinski J., Berentzen I., Shlosman I., 2009, ApJ, 697, 293
Dwek E. et al., 1995, ApJ, 445, 716
Frinchaboy P. M., Majewski S. R., Muñoz R. R., Law D. R., Łokas E. L., Kunkel W. E., Patterson R. J., Johnston K. V., 2012, ApJ, 756, 74
Gerin M., Combes F., Athanassoula E., 1990, A&A, 230, 37
Kazantzidis S., Łokas E. L., Callegari S., Mayer L., Moustakas L. A., 2011, ApJ, 726, 98
Klimentowski J., Łokas E. L., Kazantzidis S., Mayer L., Mamon G. A., 2009, MNRAS, 397, 2015
Klypin A., Valenzuela O., Colín P., Quinn T., 2009, MNRAS, 398, 1027
Lansbury G. B., Lucey J. R., Smith R., 2014, MNRAS, 439, 1749
Łokas E. L., Kazantzidis S., Majewski S. R., Law D. R., Mayer L., Frinchaboy P. M., 2010, ApJ, 725, 1516
Łokas E. L., Kazantzidis S., Mayer L., 2011, ApJ, 739, 46
Łokas E. L., Majewski S. R., Kazantzidis S., Mayer L., Carlin J. L., Nidever D. L., Moustakas L. A., 2012, ApJ, 751, 61
Łokas E. L., Gajda G., Kazantzidis S., 2013, MNRAS, 433, 878
Majewski S. R., Skrutskie M. F., Weinberg M. D., Ostheimer J. C., 2003, ApJ, 599, 1082
Martinez-Valpuesta I., Gerhard O., 2011, ApJ, 734, L20
Martinez-Valpuesta I., Shlosman I., Heller C., 2006, ApJ, 637, 214
Mayer L., Wadsley J., 2004, MNRAS, 347, 277
Mayer L., Governato F., Colpi M., Moore B., Quinn T., Wadsley J., Stadel J., Lake G., 2001, ApJ, 559, 754
Miller R. H., Smith B. F., 1979, ApJ, 227, 785
Miwa T., Noguchi M., 1998, ApJ, 499, 149
Muñoz R. R., Geha M., Willman B., 2010, AJ, 140, 138

Navarro J. F., Frenk C. S., White S. D. M., 1997, ApJ, 490, 493 (NFW)
Ohta K., Hamabe M., Wakamatsu K.-I., 1990, ApJ, 357, 71
Pfenniger D., 1984, A&A, 134, 373
Power C., Navarro J. F., Jenkins A., Frenk C. S., White S. D. M., Springel V., Stadel J., Quinn T., 2003, MNRAS, 338, 14
Raha N., Sellwood J. A., James R. A., Kahn F. D., 1991, Nature, 352, 411
Romano-Díaz E., Shlosman I., Heller C., Hoffman Y., 2008, ApJ, 687, L13
Romero-Gómez M., Athanassoula E., Antoja T., Figueras F., 2011, MNRAS, 418, 1176
Saha K., Naab T., 2013, MNRAS, 434, 1287
Saha K., Pfenniger D., Taam R. E., 2013, ApJ, 764, 123
Sellwood J. A., Athanassoula E., 1986, MNRAS, 221, 195
Sellwood J. A., Wilkinson A., 1993, Rep. Prog. Phys., 56, 173
Shen J., Rich R. M., Kormendy J., Howard C. D., De Propris R., Kunder A., 2010, ApJ, 720, L72
Sheth K. et al., 2008, ApJ, 675, 1141
Sheth K., Melbourne J., Elmegreen D. M., Elmegreen B. G., Athanassoula E., Abraham R. G., Weiner B. J., 2012, ApJ, 758, 136

Skokos Ch., Patsis P. A., Athanassoula E., 2002a, MNRAS, 333, 847
Skokos Ch., Patsis P. A., Athanassoula E., 2002b, MNRAS, 333, 861
Sparke L. S., Sellwood J. A., 1987, MNRAS, 225, 653
Springel V., 2005, MNRAS, 364, 1105
Springel V., Yoshida N., White S. D. M., 2001, New Astron., 6, 79
Stanek K. Z., Udalski A., Szymański M., Kałużny J., Kubiak Z. M., Mateo M., Krzemiński W., 1997, ApJ, 477, 163
Sundin M., Donner K. J., Sundelius B., 1993, A&A, 280, 105
Widrow L. M., Dubinski J., 2005, ApJ, 631, 838
Widrow L. M., Pym B., Dubinski J., 2008, ApJ, 679, 1239
Wills K. A., Das M., Pedlar A., Muxlow T. W. B., Robinson T. G., 2000, MNRAS, 316, 33

This paper has been typeset from a TEX/LATEX file prepared by the author.